Analyst

PAPER

View Article Online
View Journal | View Issue

Cite this: *Analyst*, 2022, **147**, 2843

Assessment of skin inflammation using near-infrared Raman spectroscopy combined with artificial intelligence analysis in an animal model†

Yohei Kanemura,‡[a,b] Meiko Kanazawa,‡[a,c] Satoru Hashimoto, ‡[d] Yuri Hayashi,[a,c] Erina Fujiwara,[d] Ayako Suzuki, [d] Takashige Ishii,[e] Masakazu Goto,[e] Hiroshi Nozaki,[e] Takanori Inoue *[d] and Hiroki Takanari *[a]

Raman spectroscopy is a powerful method for estimating the molecular structure of a target that can be adapted for biomedical analysis given its non-destructive nature. Inflammatory skin diseases impair the skin's barrier function and interfere with the patient's quality of life. There are limited methods for non-invasive and objective assessment of skin inflammation. We examined whether Raman spectroscopy can be used to predict skin inflammation with high sensitivity and specificity when combined with artificial intelligence (AI) analysis. Inflammation was chemically induced in mouse ears, and Raman spectra induced by a 785 nm laser were recorded. A principal component (PC) analysis of the Raman spectra was performed to extract PCs with the highest percentage of variance and to estimate the statistical score. The accuracy in predicting inflammation based on the Raman spectra with or without AI analysis was assessed using receiver operating characteristic (ROC) curves. We observed some typical changes in the Raman spectra upon skin inflammation, which may have resulted from vasodilation and interstitial oedema. The estimated statistical scores based on spectral changes correlated with the histopathological changes in the skin. The ROC curve based on PC2, which appeared to include some spectral features, revealed a maximum accuracy rate of 80.0% with an area under the curve (AUC) of 0.864. The AI analysis improved the accuracy rate to 93.1% with an AUC of 0.972. The current findings demonstrate that the combination of Raman spectroscopy with near-infrared excitation and AI analysis can provide highly accurate information on the pathology of skin inflammation.

Received 31st January 2022,
Accepted 21st March 2022

DOI: 10.1039/d2an00193d

rsc.li/analyst

Introduction

Raman spectroscopy is a label-free optical technique that provides structural information by detecting the wavenumber shift of scattered light after laser irradiation with a single wavelength.[1] Each substance exhibits a unique "spectral fingerprint" by vibrating patterns depending on the chemical bonds and three-dimensional structure. Raman spectroscopy has been used for physical and biological analysis in recent years.[2,3] Raman spectroscopy is a non-destructive technique that does not depend on the state of the samples, which enables the application of Raman spectroscopy to live organs. Recent studies have demonstrated that Raman spectroscopy is useful for detecting tumours,[4] myocardial infarction,[5] and β-sheet rich structure of amyloid-β protein in Alzheimer's disease.[6,7] Moreover, we have reported that Raman spectroscopy is useful for the analysis of intracellular lipids.[8] Raman spectroscopy has also been used to observe intracellular organelles.[3] These studies have suggested that Raman spectroscopy could be a powerful tool for analysing biological samples and for disease diagnosis.

The skin is an organ that covers the entire body to protect it from antigens and external factors. Inflammation in the skin is caused by allergies, infections, chemicals, and various other irritants.[9–11] Skin inflammation impairs the barrier function

[a]*Department of Interdisciplinary Researches for Medicine and Photonics, Institute of Post-LED Photonics, Tokushima University, 3-18-15, Kuramoto, Tokushima 770-8503, Japan. E-mail: takanari.hiroki@tokushima-u.ac.jp*
[b]*Tokushima University, Faculty of Science and Technology, 2-1, Minami-Josanjima, Tokushima 770-8506, Japan*
[c]*Tokushima University, Faculty of Medicine, 3-18-15 Kuramoto, Tokushima 770-8503, Japan*
[d]*Division of Applied Chemistry, Faculty of Science and Technology, Oita University Graduate School of Engineering, 700, Dan-noharu, Oita 870-1124, Japan. E-mail: tinoue@oita-u.ac.jp*
[e]*Division of DX Promotion, OEC Co., Ltd., 17-57, Higashi-Kasuga, Oita 870-0037, Japan*

†Electronic supplementary information (ESI) available. See DOI: https://doi.org/10.1039/d2an00193d

‡These authors contributed equally and share the first authorship.

of the skin and increases susceptibility to external stimuli, which causes secondary inflammation and forms a vicious circle. Inflammatory skin diseases reduce the quality of life of patients with various symptoms such as itching, pain, associated insomnia, and aesthetic problems. Diagnosis of skin diseases depends on subjective judgment, such as visual inspection and palpation by a dermatologist, which sometimes causes discrepancies between dermatologists' diagnoses and patients' complaints. Even when treating inflammatory skin diseases with topical medications, there is no method to quantitatively evaluate their therapeutic effects. In this context, research on and development of a new method to objectively evaluate the condition of the skin is required. In acute inflammation of the skin, tissue composition and components change dynamically because of inflammatory cell infiltration, interstitial oedema, and disintegration of the epidermis structure, which may be evaluated using Raman spectroscopy. However, a significant disadvantage of using Raman spectroscopy in biological samples is that it is difficult to clearly identify the substances because Raman scattering from vital organs contains miscellaneous data.

Many studies have attempted to improve the accuracy of material identification using advanced optical technologies such as coherence anti-Stokes Raman spectroscopy (CARS) and surface-enhanced Raman spectroscopy (SERS), which enhance weak Raman-scattered light from biological samples.[12,13] However, these methods are difficult to apply directly to living bodies due to problems such as the need for complicated, expensive equipment or the fact that only the surface layer of the sample can be analysed. As a workaround for this problem, we hypothesized whether we could predict inflammation through an integrated analysis of spectral characteristics of normal and inflamed tissues by decomposing Raman spectra into multiple principal components (PCs), rather than aiming to identify the individual substances such as inflammatory cytokines from Raman spectra. Recent studies have reported that the analysis of Raman spectra using artificial intelligence (AI) could be useful in elucidating pathophysiological conditions.[14,15] Therefore, we examined whether AI analysis could further improve the sensitivity and specificity of the prediction of skin inflammation through PC analysis (PCA) of Raman spectra.

Experimental

Raman spectroscopy and histological analysis in an animal model of skin inflammation

All animal experiments were approved by the Institutional Animal Care and Use Committee (approval number: T29-108) and carried out according to the Guidelines for Care and Use of Laboratory Animals of Tokushima University. Dermatitis skin lesions were induced by topical application of phorbol 12-myristate 13-acetate (PMA) on mouse ears, as described in a previous study.[16] The ears were collected before (control group) and after 6, 12, and 24 hours of PMA application (PMA-6, PMA-12, and PMA-24 groups, respectively). Thirty-one ear samples from 16 mice were divided into these four groups (control: n = 9, PMA-6: n = 7, PMA-12: n = 7, PMA-24: n = 8). Raman spectroscopy was performed using MicroRam-TE-US (Fig. S1,† Lambda Vision Inc., Sagamihara, Japan), which was controlled by the software RamanScope ver.2.62 (Lambda Vision Inc., Sagamihara, Japan). Spectroscopic data were acquired at 20 points in each ear sample (Fig. S2A†). At each measurement point, Raman spectra were recorded using one-second laser irradiation with 10-time integration. After Raman spectroscopy, ear samples were fixed with 4% paraformaldehyde, and pathological specimens were prepared for histological assessment using haematoxylin and eosin (HE) staining. The thickness of the epidermis and dermis, infiltration of inflammatory cells, vasodilation, and interstitial oedema were evaluated and scored by two or more observers, including a pathologist (Fig. S2B & C†).

Spectral data analysis, AI analysis, and statistical analysis

Raman spectra obtained from ear samples were subjected to PCA, and four major components (PC1 to PC4) that had the highest percentage of variance were extracted. Heatmap analysis and two-dimensional plot analysis were performed based on the extracted PCs. Hierarchical cluster analysis was conducted based on the combined data for PC1 to PC4 obtained in the PCA. After calculating the distance between each data point, a tree dendrogram was created based on the complete linkage method, which was used to classify the data into four clusters. Four colours (light green, dark green, dark magenta, light magenta) and scores (1 to 4) were assigned according to the distance between clusters based on the cluster containing the most data from the control group. The score was then defined as the "Raman score". Finally, receiver operating characteristic (ROC) curves were constructed to evaluate the sensitivity and specificity to predict skin inflammation based on Raman spectra.

The data were also analysed using AI. To increase the efficiency of machine learning, we added data from 63 mice (120 ear samples) included in the preliminary study. The details of the AI analysis are described in the ESI.† Briefly, all data were divided into learning and test sets as shown in Table S3,† and the learning data were further divided into 80% training data and 20% validation data. The learning model was created by training with the multilayer perceptron algorithm and validation with the validation data, which were repeated 100 times. The accuracy of normal and inflammatory predictions derived from the learning model for the test data was calculated using ROC curves (Fig. S3†).

Group data are shown as mean ± standard error of mean. Differences between group averages were tested using a one-way analysis of variance with a *post-hoc* test (Tukey's honestly significant difference) and considered significant when the p value was <0.05. A PCA of the spectral data, heatmap analysis, ROC curve analysis, and other statistical analyses were all carried out using R ver.3.6.3.[17]

Results

Inflammatory changes in the appearance of mouse ears

Representative pictures of macroscopic appearance (Fig. 1A) and histopathological images (Fig. 1B) of mouse ear samples are shown. Although erythema of the ear was not clear in the sample 6 h after the application of PMA, interstitial oedema of the skin in the PMA-6 group was confirmed through histopathological assessment. Skin erythema was visually confirmed 12 hours after PMA application. Interstitial oedema, vasodilation, and infiltration of inflammatory cells were also observed histologically (Fig. S2C†). Scab formation, blistering, and destruction and loss of epidermal tissue were apparent in the PMA-24 group, which were also visually confirmed as visible skin erosion. Results regarding the thickness of the epidermis and dermis are summarised in Fig. 1C. The epidermis gradually thickened after PMA application, and the change was particularly large 12 hours after application, which was consistent with the massive infiltration of inflammatory cells into the epidermis. Significant thickening of the dermis was observed 6 hours after PMA application, and the change thereafter was minimal, which was consistent with the time course of interstitial oedema.

Inflammation-mediated changes in Raman spectra

Three distinct peaks at wavenumbers of 1310 cm^{-1}, 1450 cm^{-1} and 1660 cm^{-1} were found in most of the Raman spectra. These spectra have also been reported in previous papers and are thought to be due to the lipid components of the skin.[18] In the inflamed skin, we frequently observed a single sharp peak at 1550 cm^{-1} followed by a bimodal peak in the wavenumber region from 1600 cm^{-1} to 1630 cm^{-1}, which occurred between the peaks of the carbon double bond of the aromatic ring at 1450 cm^{-1} and the linear carbon double bond at 1660 cm^{-1} (Fig. 2A). The former single peak was assigned to the amide-II group,[19] and the latter bimodal peak was attributed to amino acids such as phenylalanine and tyrosine.[20] These spectra coincided well with the spectrum of mouse blood (red line in Fig. 2A). We also observed a spectral change in the 2800–3000 cm^{-1} wavenumber region (Fig. 2B), which mainly represents methylene and methyl groups.[21] In normal tissues, we frequently observed CH_2-dominated spectra. In contrast, in the inflamed tissue, the signal intensity of the entire broad spectrum decreased, and its morphology appeared to change to CH_3 predominance. The mountainous spectrum in the 3100–3300 cm^{-1} wavenumber region (Fig. 2C), which represents a hydroxy group mainly derived from water (blue line in Fig. 2C), was also altered by PMA-induced skin inflammation. This spectrum was rarely observed in normal tissues and became prominent in inflamed tissues, suggesting that the spectrum represented interstitial oedema.

PCA and cluster analysis of Raman spectra

The Raman spectra obtained at each depth were subjected to PCA. Among approximately 600 PCs, PC1 to PC4—which rep-

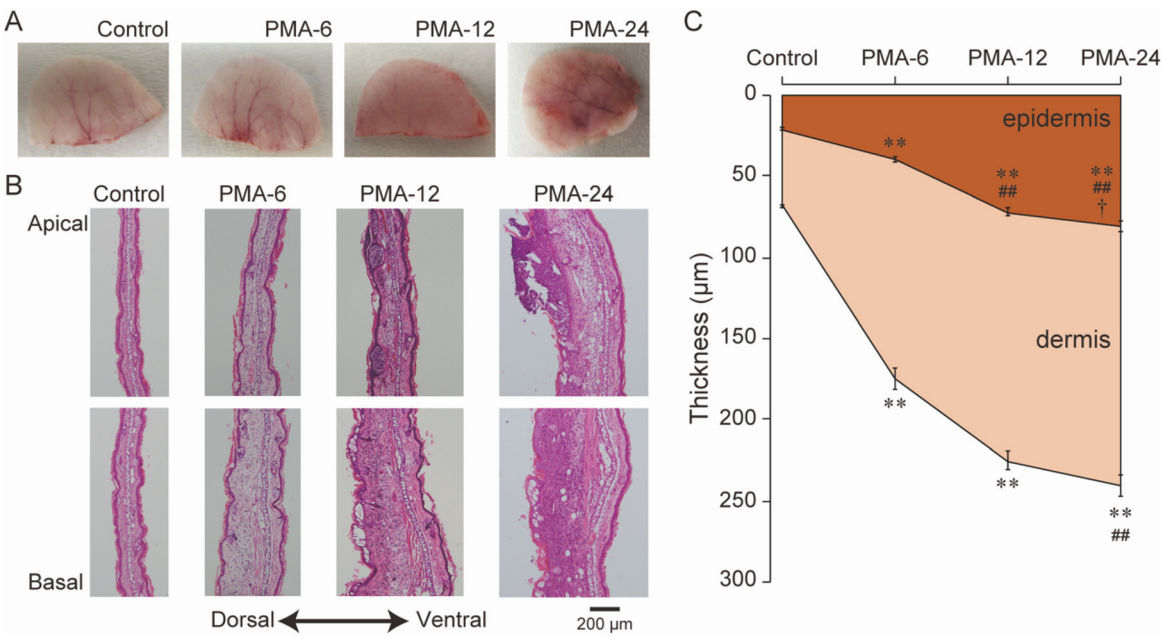

Fig. 1 Representative pictures of ear samples. (A) Macroscopic appearances of ear samples. Ears were excised before PMA application (control) or 6, 12, or 24 hours after PMA application (PMA-6, PMA-12, PMA-24, respectively). (B) Representative histological images. Ear samples were sliced and stained using haematoxylin and eosin. The left and right sides of each picture correspond to the dorsal and ventral sides of the mouse ear, respectively. The upper and lower images correspond to the apical and basal parts of each ear, respectively. (C) The thicknesses of the epidermis and dermis were measured in histological specimens from four groups and are summarised in a stacked-line chart. The brown- and ivory-coloured areas indicate the thickness of the epidermis and dermis, respectively. (**: $p < 0.01$ *vs.* control, ##: $p < 0.01$ *vs.* PMA-6, †: $p < 0.05$ *vs.* PMA-12.) PMA, phorbol 12-myristate 13-acetate.

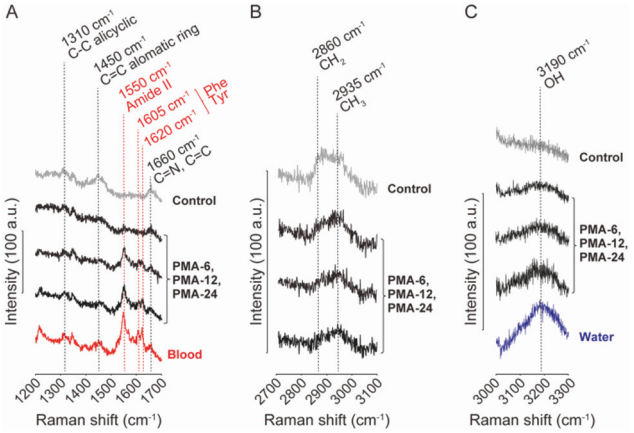

Fig. 2 Representative Raman spectra recorded from normal and inflamed tissues. The spectra recorded in normal and inflamed tissues were compared in three wave number regions: from 1400 cm^{-1} to 1700 cm^{-1} (A), from 2700 cm^{-1} to 3100 cm^{-1} (B), and from 3000 cm^{-1} to 3300 cm^{-1} (C). Spectral waveforms recorded from normal tissue, inflamed tissue, blood, and water are shown in grey, black, red, and blue, respectively. The molecular bond assigned to each wave number is indicated by vertical dotted lines. PMA, phorbol 12-myristate 13-acetate.

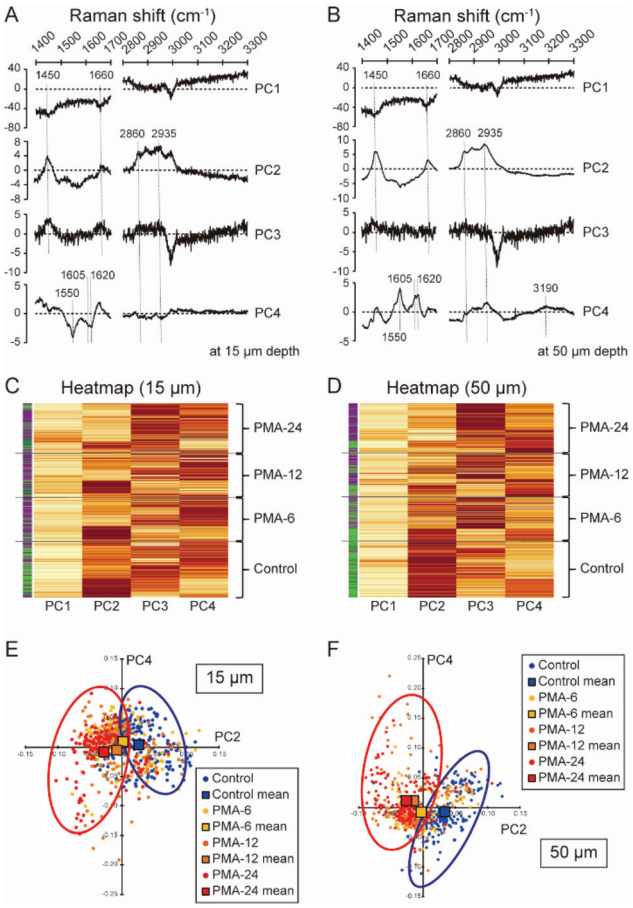

Fig. 3 Results of the principal component analysis and cluster analysis. Principal components (PCs) were extracted from Raman spectra obtained from the ear samples at depth of 15 μm (A) and 50 μm (B), and PC1 to PC4 are shown as major PCs. The vertical dotted lines indicate the positions of the peaks and their wavenumbers, which were clearly observed in each PC. A cluster analysis using a heatmap was then applied to PC1–PC4 at 15 μm (C) and 50 μm (D). Each spectrum was scored in four grades based on a cluster analysis using a dendrogram of PC1 to PC4, and the scores were assigned to colours along a gradient from light green to magenta (low to high) and displayed on the left edge of the heatmap. Data regarding the contribution of PC2 and PC4 to spectra at 15 μm (E) and 50 μm (F) are shown in a two-dimensional scatter plot. Blue, yellow, orange, and red dots indicate the plot of specific spectral data from control, PMA-6, PMA-12, and PMA-24 groups, respectively. Blue, yellow, orange, and red boxes indicate the average of contribution value for control, PMA-6, PMA-12, and PMA-24 data, respectively. The blue and red circles indicate the areas in which the data for the control group and the other three PMA-treated groups are mainly distributed, respectively. PMA, phorbol 12-myristate 13-acetate.

resented the components with the highest percentage of variance (Fig. 3A and B, variances of each PC are shown in Tables S1 and S2†)—were used for the subsequent evaluation. PC1 and PC3 appeared similar to the baseline, while PC2 appeared to contain spectral components of carbon double bonds and CH bonds. PC4 appeared to contain spectral components that could be assigned to the amide-II group and an OH bond, although the signal was inverted at 15 μm. Heatmap analysis was performed to visualise the contributions of PC1 to PC4 to the spectral data (Fig. 3C and D). The yellow-to-brick colour gradient was assigned from the lowest to the highest contribution of PC1 to PC4 to each data point. Although spatial heterogeneity and individual variations were observed, PC2 tended to exhibit a dark brick colour in the control group, while PC3 and PC4 tended to exhibit a dark brick colour in the three groups treated with PMA. We further clustered the data by composing a tree diagram according to the distance between each data point based on the contributions of PC1 to PC4. Subsequently, we derived the clustering score based on the tree diagram as the "Raman score", which was represented along a coloured gradient from green to magenta (left side of each heatmap in Fig. 3C and D). There was a tendency for data assigned to a red colour (*i.e.*, data representing a higher Raman score) to be more prominent in the inflamed skin samples. At the end of the PCA, a two-dimensional scatter plot of PC2 and PC4 was created (Fig. 3E and F). Most of the control data fell within the blue circle, and the average PC2 was positive (blue boxes). On the other hand, in the PMA-12 and PMA-24 groups, the average of the coefficient of PC2 became negative (orange and red boxes), and most data were included in the red circle. The PMA-6 group was located between the two, and the average occurred in the overlapping region of the blue and red circles. Although the direction in which the coefficient of PC4 changed at 15 μm and 50 μm was reversed, the results for the PMA-12 and PMA-24 groups (orange and red boxes) were opposite to those observed in the positive and negative control and PMA-6 groups (blue and yellow boxes).

Consistency of spectral scores and histological scores

ESI Fig. S5† shows the spatial distribution of the Raman scores as a colour map based on the cluster analysis of Raman spectra in Fig. 3C and D. In the control group, many points were assigned a green colour, which represented a lower Raman score. On the other hand, in the three PMA groups, many points were assigned a magenta colour, indicative of higher Raman scores. This tendency was more accurate for the 50 μm data. The spatial heterogeneity was averaged by calculating the mean value of the data at 20 points and using it as the data for each ear. Subsequently, the changes in the Raman score due to PMA application at 15 μm and 50 μm depth were evaluated by calculating and comparing the average score of each ear among the four groups (Fig. 4A and B, respectively). The Raman score increased significantly with PMA at both depths, although a peak of increase in the score was observed at 12 hours at the depth of 15 μm. In contrast, the score increased continuously for up to 24 hours at 50 μm.

To examine whether the changes in the Raman score reflected histological changes, HE-stained specimens were assessed for inflammatory cell infiltration, vasodilation, and oedema (Fig. 4C, D, and E, respectively). The histological score also increased significantly with PMA application in terms of all three endpoints. Especially for the infiltration of inflammatory cells, scores increased continuously for 24 hours, which was consistent with the change in the Raman score observed at 50 μm (Fig. 4B).

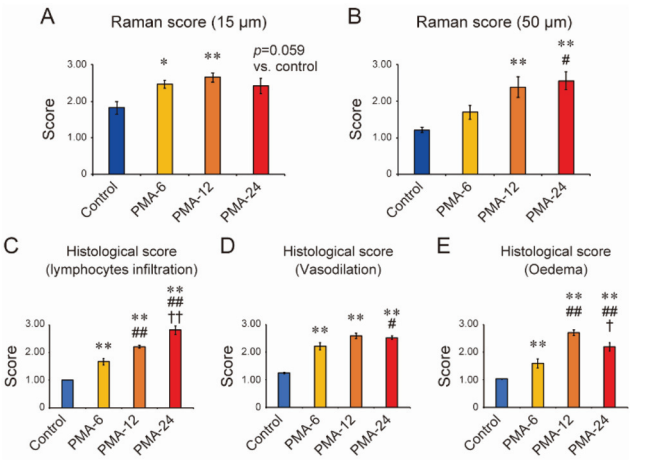

Fig. 4 Summary of Raman scores and histological scores. The average Raman scores calculated *via* principal component analysis for 20 measurement points at depths of 15 μm and 50 μm are further averaged and summarised in (A and B), respectively. Haematoxylin-and-eosin-stained sectioned tissue specimens were evaluated on a four-step scale for three items: infiltration of inflammatory cells, vasodilation, and oedema, and the averages of 20 points were calculated and are summarised in (C, D, and E), respectively. Blue, yellow, orange, and red bars represent the data for the control, PMA-6, PMA-12, and PMA-24 groups, respectively. (*: $p < 0.05$ *vs.* control, **: $p < 0.01$ *vs.* control, $^{\#}$: $p < 0.05$ *vs.* PMA-6, $^{\#\#}$: $p < 0.01$ *vs.* PMA-6, †: $p < 0.05$ *vs.* PMA-12, ††: $p < 0.01$ *vs.* PMA-12.) PMA, phorbol 12-myristate 13-acetate.

Sensitivity and specificity of Raman-based prediction of skin inflammation

We evaluated the sensitivity and specificity in predicting skin inflammation based on each PC (PC1 to PC4) at each depth (15 μm and 50 μm) using ROC curves (Fig. 5). Among them, PC2 exhibited a high accuracy rate: the ROC curve for PC2 at 15 μm yielded 74.5% accuracy with an AUC of 0.777 (Fig. 5A, the second panel), while that at 50 μm yielded the highest accuracy of 80.0%, with an AUC value of 0.864, sensitivity of 71.7%, and specificity of 83.4% when the cut-off value was set to 0.017 (Fig. 5B, second panel). The sensitivity, specificity, and accuracy of predicting inflammation even by PC2 or intensity ratio of 1550 cm^{-1}/1450 cm^{-1} (Fig. 5 and Fig. S6†), which showed a higher value for each parameter, were at a maximum of approximately 70–80%. Finally, we assessed whether AI could improve the prediction of skin inflammation based on Raman spectroscopy. Here, used the data obtained at a depth of 50 μm to construct an ROC curve (Fig. 6). The maximum accuracy for the prediction of skin inflammation increased up to 93.1%, with an AUC of 0.972. The sensitivity and specificity also improved by up to 94.6% and 89.6%, respectively.

Discussion

Optical analysis has attracted attention for its potential to promote accurate and non-invasive diagnosis in clinical medicine. Among the available methods for optical analysis, Raman spectroscopy is considered one of the most promising given that it enables non-destructive estimation of molecular structures. In this study, we investigated whether inflammation in the skin can be detected *via* Raman spectroscopy and whether Raman spectra can be used to predict the presence of skin inflammation. Our analysis identified several characteristic changes in Raman spectra associated with skin inflammation, which were considered to reflect inflammatory pathology in the skin. The PCA indicated that PC2 had a prediction accuracy of 80%, which is not accurate enough for clinical diagnosis. However, combining Raman spectroscopy with AI analysis improved the prediction accuracy to 93%. These results suggest that the combination of Raman spectroscopy and AI analysis can enable highly accurate clinical diagnosis.

In the context of clinical diagnosis, the reliability of Raman spectroscopy depends on the ability to identify the substances from which the spectra are derived. Accurate identification of substances that cause inflammation (*e.g.*, allergens, pathogens, and chemicals) and cytokines distributed in tissues secondary to inflammation may aid in diagnosing not only the presence of inflammation, but also the cause and degree of inflammation. We initially intended to detect specific inflammatory substances such as cytokines. However, although we frequently recorded spectra derived from dimethylsulfoxide, which was used as a solvent for PMA (especially in the PMA-6 group) (Fig. S7†), we were unable to discriminate any specific spectra for cytokines. In a previous study, cytokine levels in the tissue were only a few ng g^{-1}.[22] Cytokine concen-

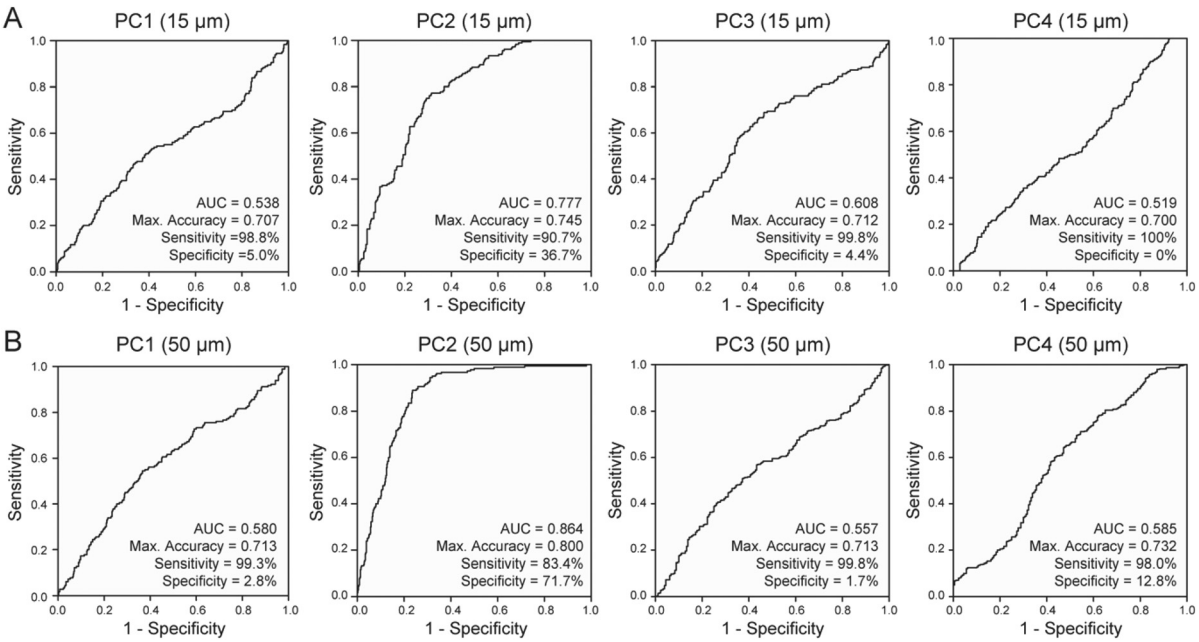

Fig. 5 ROC curves for the prediction of inflammation based on the principal components of Raman spectra. ROC curves were created to examine the sensitivity and specificity in predicting inflammation in the normal group (control group) and the inflammation group (including PMA-6, PMA-12, and PMA-24 groups) according to principal components (PCs) obtained from PC analysis based on Raman spectra obtained at the depths of 15 μm (A) and 50 μm (B). PC1 to PC4 (from left to right panel) were used to construct the ROC curves. The area under the curve (AUC) of each ROC curve, the maximum accuracy, and the sensitivity and specificity at the maximum accuracy are shown in the lower right inset of each graph. ROC, receiver operating characteristic; PMA, phorbol 12-myristate 13-acetate.

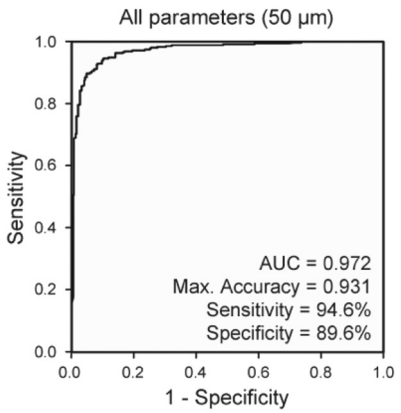

Fig. 6 ROC curve for the prediction of inflammation based on AI analysis of Raman spectra. The ROC curve was created to assess the sensitivity and specificity for predicting inflammation in the normal group (control group) and inflammation group (including PMA-6, PMA-12, and PMA-24 groups) according to AI analysis of principal components based on Raman spectra obtained at the depths of 50 μm. The area under the ROC curve (AUC), maximum accuracy, and sensitivity and specificity at the maximum accuracy are shown in the lower right inset. ROC, receiver operating characteristic; AI, artificial intelligence; PMA, phorbol 12-myristate 13-acetate.

trations in the interstitial fluid of the skin have been reported to be in the range of 50–150 pg mL^{-1} for tumour necrosis factor alpha (TNF-α) and 1–30 ng mL^{-1} for interleukin 1 beta (IL-1β).[23] Despite the development of several optical methods for enhancing faint Raman-scattered light, such as CARS and SERS,[12,13] it is still difficult to discriminate trace amounts of substances that exist in μM to nM units in tissues from other foreign substances. If a specific Raman spectrum can be used as an indicator to diagnose skin inflammation, it would be desirable to target substances that are present in the skin at higher concentrations[21] or that have extremely distinctive and sharp spectra, such as lipids or phospholipids.[24]

Although we could not identify inflammation-specific substances such as cytokines, we did observe several inflammation-induced changes in the Raman spectra. The newly-emerged spectra in the 1500–1650 cm^{-1} region were consistent with the Raman spectrum of haem protein,[25] which we considered to represent vasodilation due to skin inflammation. Inflammation decreased the peaks observed at 1450 cm^{-1} and 1660 cm^{-1} for carbon double bonds, which are frequently observed in Raman spectroscopy of living cells or organs and are considered to represent fats or membrane phospholipids.[18] Attenuation of these two peaks may indicate a decrease in the lipid barrier of the skin or changes in cellular composition due to interstitial oedema. We also observed broad-spectrum morphological changes at 2800–3000 cm^{-1}, which were assigned to the stretch of CH bonds. This result is consistent with the changes previously observed in rat skin infected with *Fusarium oxysporum*,[26] suggesting that inflammation altered lipid and protein composition in the skin. Water is among the molecules most commonly analysed in Raman spectroscopy of the skin.[27] We observed spectral elevation at 3190 cm^{-1}, which

can be explained by an increase in the interstitial water content due to tissue oedema.

Even though each change in the Raman spectra can explain the pathological changes caused by skin inflammation, the intensity ratio of individual spectra did not exhibit high sensitivity or specificity for predicting inflammation (Fig. S6†). Therefore, we performed PCA to examine the series of spectral changes, rather than verifying specific spectral changes one by one. Although it may not be possible to determine the exact substances responsible for changes in the Raman spectra, it should be possible to distinguish between normal and diseased tissues by analysing multiple factors in combination. Among the extracted PCs, PC2 appeared to contain spectra of carbon double bonds and CH bonds, which may have been derived from phospholipids.[18] The ROC curve created based on PC2 showed relatively high accuracy in predicting skin inflammation (Fig. 5, the second panels from the left), although the rate was insufficient for clinical diagnosis. The ROC curve based on PC4, which appeared to involve spectra for the amide-II group (representing vasodilation) and an OH bond (representing interstitial oedema), did not have sufficient power to predict skin inflammation (Fig. 5, the rightmost panels). The percentage of variance was very small for PC2 and PC4, indicating that they may not have contributed sufficiently to the changes in the overall Raman spectrum (Tables S1 & S2†). On the other hand, PC1, which contained baseline and noise components, occupied more than 95% of the variance. Individual differences among mice, spatial heterogeneity within each sample, and even temporal heterogeneity in the progression of inflammation progression may have maximized the variance of PC1 and reduced the relative variance due to PC2 and PC4. This also made it impossible to determine the degree of inflammation over time, as originally intended.

If Raman spectroscopy is to be applied in clinical practice, the above problems, such as faint and complex changes in diverse components and individual differences, must be overcome. For such comprehensive comparisons, machine learning and AI-based analysis will be of significant help. In fact, in our study, the prediction accuracy for inflammation based on PCs was at best 80%; however, addition of AI analysis increased the prediction accuracy to 93%. Although the reason for this improvement remains unclear, it is likely due to the elimination of individual differences among mice and the temporal and spatial heterogeneity of inflammatory responses, allowing for increased sensitivity. In the future, the introduction of explainable AI may help to improve the accuracy of diagnosis. Several recent studies have verified that AI can be applied in various areas of clinical medicine and medical research.[14,15] In the dermatological field, Esteva *et al.* reported that high diagnostic accuracy based on a macroscopic view of skin lesions achieved using a deep-neural network system.[28]

Although the presence of inflammation could be diagnosed in the present study, our method was unable to determine degree of inflammation. As both factors are essential for diagnosing inflammatory skin diseases in clinical settings, this represents a major limitation of the study. We initially aimed to verify whether the degree of inflammation could be determined by analysing samples at different time points after PMA application. However, the number of samples was too small to determine the degree of inflammation. Furthermore, skin diseases are not limited to dermatitis, but also include tumours, metabolic abnormalities, pigmentation abnormalities, and hair-growth abnormalities. To identify these diseases, large amounts of clinical data and complex AI algorithms are required. Nonetheless, the current findings highlight the potential of Raman spectroscopy combined with AI analysis to aid in the non-invasive diagnosis of skin diseases.

Among the major barriers to applying Raman spectroscopy in clinical medicine are the limitations in the depth that can be reached and the ability to detect Raman-scattered light from deep tissues. Ultrasound-based technology enables the evaluation of deep skin tissue up to approximately 4 cm,[29] and studies have revealed that ultrasonic Doppler can be used to detect tumour angiogenesis.[30] While ultrasound technology is thus suitable for obtaining certain information in deep tissues it cannot provide information regarding the molecular properties of the area. If its penetrative ability can be improved, Raman spectroscopy will represent a powerful *in vivo* diagnostic tool. Researchers have proposed the use of near-infrared light to address this issue.[31] In general, longer wavelengths of light penetrate tissues more deeply. In this study, we used a near-infrared laser with a wavelength of 785 nm instead of the 532 nm laser that is commonly used in Raman spectroscopy to irradiate deeper areas, and we confirmed that Raman-scattered light could be detected up to a depth of 250 μm with an exposure time of one second (Fig. S8†). Since the thickness of the human epidermis is around 100–200 μm,[32] our results suggest that epidermal lesions can be detected using a 785 nm laser.

Conclusions

We demonstrated the changes in the Raman spectrum induced by skin inflammation, which were considered to reflect vasodilation and interstitial oedema. Although it was still difficult to accurately predict the presence or absence of inflammation from individual changes in Raman spectra, it was possible to improve the prediction accuracy to some extent by considering multiple spectra in a combined manner using PCA. By combining with AI, it has shown the possibility of an objective evaluation of skin inflammation using Raman spectroscopy.

Data availability

The data that support the findings of this study are available from the corresponding authors upon request.

Author contributions

Y. K.: investigation, formal analysis, writing-Original draft. M. K.: investigation, formal analysis, writing-original draft. S. H.: con-

ceptualization, writing-review & editing. Y. H.: investigation, validation. E. F.: investigation, validation. A. S.: validation, writing-review & editing. T. I.: software, methodology. M. G.: software, validation. H. N.: software, validation. T. I.: conceptualization, methodology, supervision, project administration. H. T.: conceptualization, investigation, formal analysis, writing-review & editing, project administration, funding acquisition.

Conflicts of interest

This study was partially funded by Astellas Pharma Inc. The sponsor had no control over the interpretation of the data, writing, or publication of this work.

Acknowledgements

We thank Dr Takeshi Terabayashi from the Department of Pharmacology, Oita University School of Medicine, for advice and practical instructions regarding the development of the PMA-induced dermatitis model in mouse ears. We also thank Dr Takeshi Oya from the Department of Pathology and Laboratory Medicine, Tokushima University, for providing mouse ear specimens for pathological assessment. This work was supported by the JSPS KAKENHI (grant numbers JP16H05238 [H. T.] and JP19H04443 [H. T.]).

References

1 C. V. Raman and K. S. Krishnan, *Nature*, 1928, **122**, 12–13.
2 H. J. Butler, L. Ashton, B. Bird, G. Cinque, K. Curtis, J. Dorney, K. Esmonde-White, N. J. Fullwood, B. Gardner, P. L. Martin-Hirsch, M. J. Walsh, M. R. McAinsh, N. Stone and F. L. Martin, *Nat. Protoc.*, 2016, **11**, 664–687.
3 B. Durrant, M. Trappett, D. Shipp and I. Notingher, *Curr. Opin. Chem. Biol.*, 2019, **51**, 138–145.
4 K. Kong, C. J. Rowlands, S. Varma, W. Perkins, I. H. Leach, A. A. Koloydenko, H. C. Williams and I. Notingher, *Proc. Natl. Acad. Sci. U. S. A.*, 2013, **110**, 15189–15194.
5 T. Yamamoto, T. Minamikawa, Y. Harada, Y. Yamaoka, H. Tanaka, H. Yaku and T. Takamatsu, *Sci. Rep.*, 2018, **8**, 14671.
6 V. Shashilov, M. Xu, N. Makarava, R. Savtchenko, I. V. Baskakov and I. K. Lednev, *J. Phys. Chem. B*, 2012, **116**, 7926–7930.
7 L. A. Popova, R. Kodali, R. Wetzel and I. K. Lednev, *J. Am. Chem. Soc.*, 2010, **132**, 6324–6328.
8 T. Minamikawa, M. Ichimura-Shimizu, H. Takanari, Y. Morimoto, R. Shiomi, H. Tanioka, E. Hase, T. Yasui and K. Tsuneyama, *Sci. Rep.*, 2020, **10**, 18548.
9 F. Huet, M. Severino-Freire, J. Cheret, O. Gouin, J. Praneuf, O. Pierre, L. Misery and C. Le Gall-Ianotto, *J. Dermatol. Sci.*, 2018, **89**, 213–218.
10 T. E. Woo, R. Somayaji, R. M. Haber and L. Parsons, *Adv. Skin Wound Care*, 2019, **32**, 542–549.
11 D. Mohania, S. Chandel, P. Kumar, V. Verma, K. Digvijay, D. Tripathi, K. Choudhury, S. K. Mitten and D. Shah, *Adv. Exp. Med. Biol.*, 2017, **996**, 71–87.
12 C. H. Camp, Jr., Y. J. Lee, J. M. Heddleston, C. M. Hartshorn, A. R. Hight Walker, J. N. Rich, J. D. Lathia and M. T. Cicerone, *Nat. Photonics*, 2014, **8**, 627–634.
13 Y. Lai, S. Schlücker and Y. Wang, *Anal. Bioanal. Chem.*, 2018, **410**, 5993–6000.
14 I. U. Rehman, R. S. Khan and S. Rehman, *Expert Rev. Mol. Diagn.*, 2020, **20**, 749–755.
15 R. Kothari, V. Jones, D. Mena, V. Bermúdez Reyes, Y. Shon, J. P. Smith, D. Schmolze, P. D. Cha, L. Lai, Y. Fong and M. C. Storrie-Lombardi, *Sci. Rep.*, 2021, **11**, 6482.
16 K. Sato, M. Takaishi, S. Tokuoka and S. Sano, *PLoS One*, 2014, **9**, e112408.
17 R Core Team, *R: A language and environment for statistical computing*, R Foundation for Statistical Computing, Vienna, Austria, 2020.
18 F. Boschetto, T. Adachi, S. Horiguchi, D. Fainozzi, F. Parmigiani, E. Marin, W. Zhu, B. McEntire, T. Yamamoto, N. Kanamura, O. Mazda, E. Ohgitani and G. Pezzotti, *J. Biomed. Opt.*, 2018, **23**, 1–10.
19 K. Xiong, D. Punihaole and S. A. Asher, *Biochemistry*, 2012, **51**, 5822–5830.
20 J. R. A. Moreno, M. d. M. Q. Moreno, F. P. Ureña and J. J. LópezGonzález, *Tetrahedron: Asymmetry*, 2012, **23**, 1084–1092.
21 P. J. Caspers, G. W. Lucassen, E. A. Carter, H. A. Bruining and G. J. Puppels, *J. Invest. Dermatol.*, 2001, **116**, 434–442.
22 N. Prince, J. A. Penatzer, T. L. Shackleford, E. K. Stewart, M. J. Dietz and J. W. Boyd, *J. Orthop. Res.*, 2021, **39**, 2159–2168.
23 T. Nedrebø, R. K. Reed, R. Jonsson, A. Berg and H. Wiig, *J. Physiol.*, 2004, **556**, 193–202.
24 A. Kováčik, P. Pullmannová, L. Pavlíková, J. Maixner and K. Vávrová, *Sci. Rep.*, 2020, **10**, 3832.
25 R. Gautam, J. Y. Oh, R. P. Patel and R. A. Dluhy, *Analyst*, 2018, **143**, 5950–5958.
26 M. H. Correia, F. Sato, M. L. Baesso, A. C. Bento, M. S. Gibin, G. R. de Moraes, K. S. Melo, T. I. E. Svidzinski, G. Almeida, C. A. B. Amado and L. Hernandes, *Spectrochim. Acta, Part A*, 2020, **234**, 118246.
27 P. J. Caspers, G. W. Lucassen, H. A. Bruining and G. J. Puppels, *J. Raman Spectrosc.*, 2000, **31**, 813–818.
28 A. Esteva, B. Kuprel, R. A. Novoa, J. Ko, S. M. Swetter, H. M. Blau and S. Thrun, *Nature*, 2017, **542**, 115–118.
29 J. Czajkowska, S. Korzekwa and E. Pietka, *Comput. Med. Imaging Graph.*, 2020, **79**, 101676.
30 G. Lancaster, A. Stefanovska, M. Pesce, G. Marco Vezzoni, B. Loggini, R. Pingitore, F. Ghiara, P. Barachini, G. Cervadoro, M. Romanelli and M. Rossi, *Sci. Rep.*, 2015, **5**, 12825.
31 N. Kourkoumelis, I. Balatsoukas, V. Moulia, A. Elka, G. Gaitanis and I. D. Bassukas, *Int. J. Mol. Sci.*, 2015, **16**, 14554–14570.
32 P. Oltulu, B. Ince, N. Kokbudak, S. Findik and F. Kilinc, *Turk. J. Plast. Surg.*, 2018, **26**, 56–61.